ENVIRONMENTAL RESEARCH

LETTERS

LETTER • OPEN ACCESS

Evaluating photosynthetic activity across Arctic-Boreal land cover types using solar-induced fluorescence

To cite this article: Rui Cheng et al 2022 Environ. Res. Lett. 17 115009

View the article online for updates and enhancements.

You may also like

- Missing pieces to modeling the Arctic-Boreal puzzle
 Joshua B Fisher, Daniel J Hayes, Christopher R Schwalm et al.
- Exposure to cold temperature affects the spring phenology of Alaskan deciduous vegetation types Mingjie Shi, Nicholas C Parazoo, Su-Jong Jeong et al.
- Soil respiration strongly offsets carbon uptake in Alaska and Northwest Canada Jennifer D Watts, Susan M Natali, Christina Minions et al.

ENVIRONMENTAL RESEARCH

LETTERS



OPEN ACCESS

RECEIVED

15 July 2022

REVISED

16 October 2022

ACCEPTED FOR PUBLICATION 26 October 2022

9 November 2022

Original Content from this work may be used under the terms of the Creative Commons Attribution 4.0 licence.

Any further distribution of this work must maintain attribution to the author(s) and the title of the work, journal citation and DOI.



LETTER

Evaluating photosynthetic activity across Arctic-Boreal land cover types using solar-induced fluorescence

Rui Cheng^{1,13,*}, Troy S Magney², Erica L Orcutt², Zoe Pierrat⁸, Philipp Köhler⁷, David R Bowling³, M Syndonia Bret-Harte⁴, Eugénie S Euskirchen⁴, Martin Jung⁵, Hideki Kobayashi⁶, Adrian V Rocha⁹, Oliver Sonnentag¹⁰, Jochen Stutz⁸, Sophia Walther⁵, Donatella Zona¹¹ and Christian Frankenberg^{1,12}

- Division of Geological and Planetary Sciences California Institute of Technology, Pasadena 91125, CA, United States of America
- Department of Plant Sciences, University of California, Davis 95616, CA, United States of America
- ³ School of Biological Sciences, University of Utah, Salt Lake City 84112, UT, United States of America
- Institute of Arctic Biology and Department of Biology and Wildlife, University of Alaska, Fairbanks 99775, AK, United States of America
- Department of Biogeochemical Integration, Max Planck Institute for Biogeochemistry, Jena 07745, Germany
- ⁶ JAMSTEC-Japan Agency for Marine-Earth Science and Technology, 3173-25, Showa-machi, Kanazawa-ku, Yokohama 236-0001, Kanagawa, Japan
- EUMETSAT, Darmstadt D-64295, Germany
- Department of Atmospheric and Oceanic Sciences, University of California, Los Angeles 90095, CA, United States of America
- Department of Biology, University of Notre Dame, Notre Dame 46556, IN, United States of America
- Département de géographie, Université de Montréal, Montréal H2V 2B8, Québec, Canada
- Department Biology, San Diego State University, San Diego 92182, CA, United States of America
- Jet Propulsion Laboratory, California Institute of Technology, Pasadena 91109, CA, United States of America
- Department of Civil and Environmental Engineering, Massachusetts Institute of Technology, Cambridge 02139, MA, United States of America
- * Author to whom any correspondence should be addressed.

E-mail: rui.cheng@caltech.edu

Keywords: solar-induced chlorophyll fluorescence (SIF), FluxCom GPP, snow, surface water, Arctic land cover, topography

Abstract

Photosynthesis of terrestrial ecosystems in the Arctic-Boreal region is a critical part of the global carbon cycle. Solar-induced chlorophyll Fluorescence (SIF), a promising proxy for photosynthesis with physiological insight, has been used to track gross primary production (GPP) at regional scales. Recent studies have constructed empirical relationships between SIF and eddy covariance-derived GPP as a first step to predicting global GPP. However, high latitudes pose two specific challenges: (a) Unique plant species and land cover types in the Arctic-Boreal region are not included in the generalized SIF-GPP relationship from lower latitudes, and (b) the complex terrain and sub-pixel land cover further complicate the interpretation of the SIF-GPP relationship. In this study, we focused on the Arctic-Boreal vulnerability experiment (ABoVE) domain and evaluated the empirical relationships between SIF for high latitudes from the TROPOspheric Monitoring Instrument (TROPOMI) and a state-of-the-art machine learning GPP product (FluxCom). For the first time, we report the regression slope, linear correlation coefficient, and the goodness of the fit of SIF-GPP relationships for Arctic-Boreal land cover types with extensive spatial coverage. We found several potential issues specific to the Arctic-Boreal region that should be considered: (a) unrealistically high FluxCom GPP due to the presence of snow and water at the subpixel scale; (b) changing biomass distribution and SIF-GPP relationship along elevational gradients, and (c) limited perspective and misrepresentation of heterogeneous land cover across spatial resolutions. Taken together, our results will help improve the estimation of GPP using SIF in terrestrial biosphere models and cope with model-data uncertainties in the Arctic-Boreal region.

1. Introduction

As a critical part of the global carbon cycle and land carbon sink for atmospheric CO2, terrestrial photosynthesis in the Arctic-Boreal region can play a key role in mitigating global climate change (Beer et al 2010, Mishra and Riley 2012). Due to exceedingly high warming trends at high latitudes (Post et al 2019, Walsh and Brettschneider 2019), Arctic-Boreal ecosystems are undergoing more rapid changes than the rest of the world (Box et al 2019, Canadell et al 2021), such as in photosynthetic productivity, growing season phenology, and vegetation composition (Myers-Smith et al 2020). As a result, the future direction and magnitude of terrestrial ecosystem change in these systems has become highly uncertain (McGuire et al 2009, Loisel et al 2021, Zona et al 2022). To better evaluate climate impacts on the Arctic-Boreal region and understand vegetation-climate feedbacks, monitoring the status of Arctic-Boreal terrestrial photosynthesis is essential (Fisher et al 2014).

Plant carbon uptake via photosynthesis at the ecosystem scale, gross primary production (GPP), can only be estimated indirectly from the ground or space. On the ground, tower-based eddy covariance (EC) techniques directly measure net ecosystem CO₂ exchange (Baldocchi 2003), which is then partitioned into GPP and ecosystem respiration. EC towers in the Arctic-Boreal region are unevenly and sparsely distributed in space (figure 1, table 1), which make it difficult to represent the spatial variability of GPP across heterogeneous land cover in the Arctic-Boreal region (Curasi et al 2022, Pallandt et al 2022). EC techniques are also prone to error in complex terrain, which plays an important role in above-ground biomass distributions in the Arctic-Boreal region (Bruun et al 2006, Dobrowski 2011, Riihimäki et al 2017).

Similar to EC towers, satellite remote sensing techniques indirectly infer GPP. An advantage of satellite remote sensing techniques is a more extensive spatial coverage, enabling the comparison of GPP across heterogeneous land cover (Funk *et al* 2004, Roland *et al* 2021) and complex Arctic-Boreal terrain (Roland *et al* 2019). However, satellite remote sensing techniques also have higher uncertainties due to more assumptions made in the derivation of GPP (Tramontana *et al* 2015, Ryu *et al* 2019).

Remote sensing techniques often rely on canopy optical properties that can approximate absorbed photosynthetic active radiation (APAR) by vegetation. The fraction of APAR used for photosynthesis is referred to as light use efficiency (LUE). So, GPP can be derived as

$$GPP = APAR \times LUE. \tag{1}$$

Remote sensing GPP products, such as from the moderate resolution imaging spectroradiometer (MODIS) (Running *et al* 2004, Zhao *et al* 2005), are primarily derived from the normalized difference in the surface reflectance between red and near-infrared regions, which is a proxy for the fraction of incoming light absorbed by the canopy, or APAR. However, APAR changes alone are not representative of the seasonal cycle in boreal evergreen ecosystems well, as vegetation photosynthetic activity ceases while maintaining light absorbing chlorophyll throughout the season (Bowling *et al* 2018, Magney *et al* 2019, Cheng *et al* 2020). Thus, quantifying variations in LUE is crucial for accurately estimating Arctic-Boreal GPP.

Remote sensing of solar-induced chlorophyll fluorescence (SIF) from space opens up a new possibility to infer GPP remotely (Frankenberg *et al* 2011, Guanter *et al* 2012, Sun *et al* 2017, Li *et al* 2018, Zhang *et al* 2020, Turner *et al* 2021, Li and Xiao 2022). SIF is a small amount of energy emitted from leaf chlorophyll, which is driven by APAR. SIF appears to be a good indicator of the partitioning of APAR between photochemical quenching for photosynthesis and non-photochemical quenching, i.e. LUE (Magney *et al* 2019, Pierrat *et al* 2022), especially in challenging environments that are snowy or have low solar angles (Walther *et al* 2016, 2018). Thus, satellite-based SIF is a promising tool for inferring GPP at the regional scale in the Arctic-Boreal region.

Similar to equation (1), SIF can be conceptualized as:

$$SIF = APAR \times \Phi_F \times f_{esc}, \qquad (2)$$

where Φ_F is the quantum yield of fluorescence, and $f_{\rm esc}$ is the escape ratio of SIF from the canopy (Guanter et al 2014, Zeng et al 2019). To predict GPP using SIF, recent studies (Zhang et al 2020, Turner et al 2021, Li and Xiao 2022) have built an empirical linear model between daily mean GPP from EC towers and daily mean SIF (SIF_{dc}) from the TROPOspheric Monitoring Instrument (TROPOMI; Köhler et al 2018), assuming linearity between SIF_{dc} and GPP (Turner et al 2021, Liu et al 2022):

$$GPP = k \cdot SIF_{dc}. \tag{3}$$

Thus, the regression slope k can be generalized in different plant functional types to account for varying photosynthetic yields, SIF yields, and canopy structures since it is a function of LUE, Φ_F , and $f_{\rm esc}$:

$$k \sim \frac{\text{LUE}}{\Phi_F \times f_{\text{esc}}},$$
 (4)

Solving and categorizing k by plant functional types has improved the ability of biosphere models to simulate GPP in temperate regions (Delaria $et\ al\ 2021$, Wu $et\ al\ 2021$). However, the resulting k values from previous studies (Turner $et\ al\ 2021$, Li and Xiao 2022, Liu $et\ al\ 2022$) lack representativeness in the Arctic-Boreal region because they are categorized by general definitions of plant functional types at the global scale, rather than being tuned to the unique

vegetation composition and land cover in the Arctic-Boreal region.

Hence, the goal of this study is to quantitatively evaluate the empirical SIF-GPP relationship (equation (3)) and its uncertainty in the context of the Arctic-Boreal region at the regional scale using remote sensing techniques. We chose to focus on the core region Arctic-Boreal vulnerability experiment (ABoVE) domain (www.above.nasa.com; Goetz et al 2011, Griffith et al 2012, Loboda et al 2017), where land cover types have been defined and validated in the context of Arctic-Boreal species and canopy structures (figure 1(a); Wang et al 2019). To obtain extensive spatial coverage we fit the empirical SIF-GPP relationship and solved for k using TROPOMI SIF_{dc} and a state-of-the-art machine learning gridded GPP product (FluxCom RS; Jung et al 2020). To help biosphere modelers cope with the model-data uncertainties (Keenan et al 2011, Xiao et al 2014), we evaluated the goodness of empirically fitted SIF-GPP relationships with Pearson's r^2 values and reduced χ^2 given the uncertainties in both FluxCom GPP and TROPOMI SIF_{dc}.

Even though the gridded products are advantageous at regional scales in the Arctic-Boreal regions, the potential systematic biases of gridded products can complicate the understanding of the SIF-GPP relationship (Sun *et al* 2017). Thus, we addressed four other sources of uncertainties in the SIF-GPP relationship: (a) selection of gridded products, (b) snow contamination in remote sensing products, (c) changing biomass distribution along elevational gradients, and (d) limited perspective and misrepresentation of heterogeneous land cover across spatial resolutions. Here, we present the opportunities and limitations of remote sensing and machine learning tools for studying GPP in the Arctic-Boreal region (section 4.1).

2. Data and methods

2.1. Gridded datasets and their uncertainties

2.1.1. FluxCom GPP

We used the ensemble median of 2018-2019 eightday GPP from the FluxCom remote sensing (RS) ensembles (Tramontana et al 2016, Jung et al 2020) with a spatial resolution of $0.08333^{\circ} \times 0.08333^{\circ}$. FluxCom RS ensembles include 18 members from nine machine learning models and two GPP flux partitioning methods. Using GPP from EC towers as training data (Tramontana et al 2016), all ensemble members of different methods predict GPP with the same set of predictors, including land surface temperature, land cover, the fraction of absorbed photosynthetically active radiation, and normalized difference vegetation index (NDVI) from MODIS land products. We took the standard deviation of the predicted GPP of all ensembles as the uncertainty of FluxCom GPP.

Because the FluxCom RS GPP is predicted by remote sensing products, snow contamination in MODIS products (Cihlar 1996) can propagate into FluxCom GPP. To evaluate the impact of snow contamination on the SIF-GPP relationship, we compared the seasonal trajectory of FluxCom GPP with and without snow filtering. We used the 2018–2019 eight-day MODIS L3 0.05° global snow cover product MOD10C2 (Hall and Riggs 2021) as a snow filter, which reports the area fraction of snow cover (dimensionless) in each grid cell. The snow cover data in the study area were regridded to the same spatial and temporal resolution as the FluxCom GPP product. Here, we define FluxCom GPP as snow-free when the snow cover is less than 0.1 (figure B.6).

Additionally, the uncertainty of FluxCom GPP can be also due to the extrapolation of trained parameters due to limited EC towers sampling. Jung *et al* (2020) has developed an extrapolation index (EI) to address this issue by illustrating the total distance of an extrapolated point to the nearest training data in the space of all predictors. Here, we reproduced the multi-year average (2001–2018) of annual mean EI and its seasonal range in the study domain to qualitatively examine the representativeness of FluxCom GPP.

2.1.2. TROPOMI SIF

We gridded individual SIF soundings from TRO-POMI at 740 nm between 2018 and 2019 in the study area to the same spatial and temporal resolutions as FluxCom GPP (appendix A). Because satellite-based SIF is an instantaneous value indicative of the light condition at the time of measurement, the daily mean SIF, SIF_{dc}, was scaled from the instantaneous measurement using a length-of-day correction factor based on the diurnal cycle of solar radiation (Köhler *et al* 2018). To account for varying numbers of soundings across grids, we took the standard error of SIF_{dc} from individual soundings falling in each grid cell as the uncertainty of TROPOMI SIF, which is derived as the standard deviation divided by the square root of the number of soundings.

2.1.3. Orthogonal distance regression

With snow-free FluxCom GPP and TROPOMI SIF_{dc} as well as their uncertainties, we fit the linear model in equation (3) without an intercept using the orthogonal distance regression (Boggs *et al* 1989) for each grid cell, where the regression slope k, Pearson's r^2 , and reduced χ^2 were computed.

Previous studies (Liu *et al* 2022, Wu *et al* 2022) have often used Pearson's r^2 as the only metric for explanatory power even though measurement noise can reduce Pearson's r^2 , although the measurements themselves might be accurate but just less precise. Thus, we use both Pearson's r^2 and reduced χ^2 together to evaluate the linear empirical model

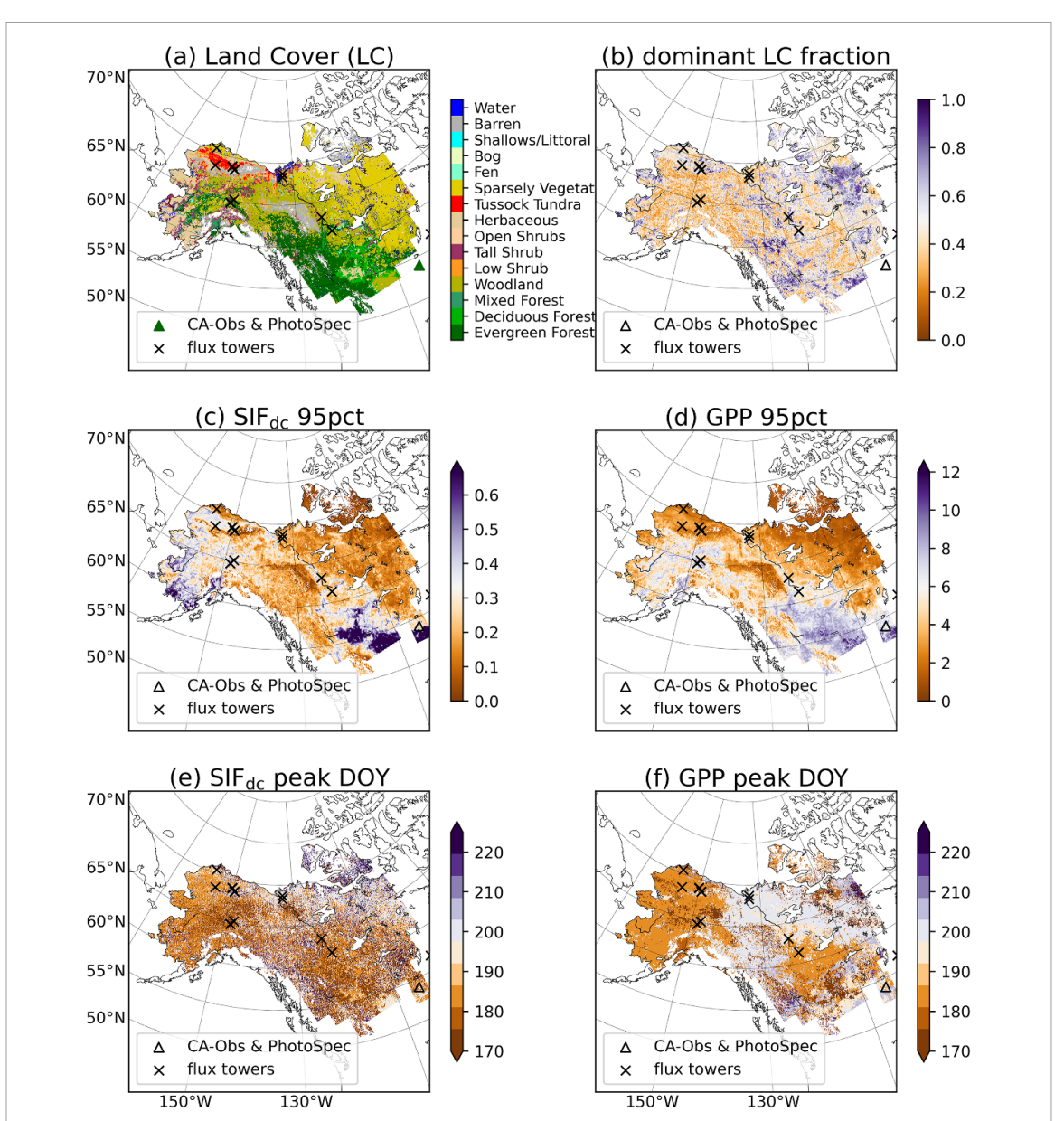


Figure 1. In the study area (core region of the Arctic-Boreal vulnerability experiment (ABoVE) domain) and the resolution of $0.083~33^{\circ} \times 0.083~33^{\circ}$: (a) the dominant land cover types (Wang et al 2019); (b) the area fraction of grid taken by the dominant land cover types in panel (a); (c) the 95 percentile of SIF_{dc} (mW m⁻² sr⁻¹ nm⁻¹); (d) the 95 percentile of snow-free FluxCom GPP (gC m⁻² day⁻¹); (e) the day of year when SIF_{dc} peaks; and (f) the day of year when GPP peaks. The black cross scatters show the locations of eddy covariance (EC) towers with GPP data within the ABoVE land cover map. The triangle scatter denotes the location of Saskatchewan-Western Boreal, Mature Black Spruce site (CA-Obs) which has both GPP data and tower-based SIF data. In (a) the triangle scatter is colored in dark green to show that the land cover type of CA-Obs footprint is Evergreen Forest. In (c)–(f), the maps are extended to the area surrounding CA-Obs since data are available. The 95 percentiles were chosen based on the relationship of ranking, percentile, and the number of samples.

between GPP and SIF_{dc} from the perspective of correlation (Pearson's r^2) as well as the goodness of the fit (reduced χ^2). High reduced χ^2 suggests the linear model is underfitting the data. When reduced χ^2 is lower than 1, it suggests that the linear model is overfitting the given uncertainties on FluxCom GPP and grid TROPOMI SIF_{dc}. A reduced χ^2 around 1 represents a good fit, regardless of Pearson's r^2 value.

2.1.4. Arctic-Boreal land cover map

In the context of Arctic-Boreal species and canopy structures, we categorized the fitted k, Pearson's r^2 , and reduced χ^2 by 15 Arctic-Boreal land cover types

based on 2014 ABoVE Land Cover dataset from (Wang *et al* 2019). The original spatial resolution of the land cover dataset is $30 \text{ m} \times 30 \text{ m}$ (LC30M), which we aggregated into $0.083 \, 33^{\circ} \times 0.083 \, 33^{\circ}$ (LC008333D) grids to align with FluxCom GPP. The land cover pixels of LC30M were counted within each LC008333D grid. The land cover type with the maximal area fraction in the LC008333D grid is defined as the dominant land cover type (figure 1(a)), while the maximal area fraction is defined as the dominant land cover fraction (figure 1(b)). Heterogeneous land cover is associated with a lower dominant land cover fraction.

Surface water is common in Arctic-Boreal ecosystems (Stow et al 2004, Muster et al 2013). However, NDVI obtained from mixed pixels including both vegetation and surface water is often close to that of vegetation only. Because water surfaces are very dark (Jiang et al 2005), few of the reflected photons measured from space emanate from water surfaces. To estimate the influence of the underestimated surface water on FluxCom GPP which uses NDVI (Tramontana et al 2016), we calculated the area fraction per LC008333D grid occupied by wetland land cover types including Fen, Bog, and Water. Here, we neglected Shallows/littoral land cover type as it is nonvegetation dominated and dominates less than 0.1% of all LC008333D grids.

2.2. Topography

We decomposed the resulting k, Pearson's r^2 , and reduced χ^2 as a function of elevation. The elevation data in the study area were obtained from the USGS Global 30 Arc-Second elevation dataset (GTOPO30; Earth Resources Observation And Science (EROS) Center 2017). We regridded the elevation data to the same spatial resolution as FluxCom GPP using Google Earth Engine (Gorelick *et al* 2017).

2.3. Ground-level GPP and SIF

Due to highly heterogeneous land cover (Myers-Smith *et al* 2020, Wang *et al* 2020) in the Arctic-Boreal region, the SIF-GPP relationships at different observational scales can vary. Satellite footprints often cover a larger area than the footprints of EC towers so the dominant land cover of the two scales may not match despite the satellite footprints centering on the location of towers. To address the difference and correspondence across scales, we compared the observations from towers against satellite pixels of the same land cover types.

We used half-hourly gap-filled GPP data of EC towers from principal investigators (PIs) and the Fluxnet2015 dataset (Papale *et al* 2015; table 1) in the study area and calculated the daily mean EC GPP. Because of various temporal ranges for different towers, we calculated the multi-year average of daily mean EC GPP at the eight-day interval aligned with the temporal interval of FluxCom GPP. We defined the land cover types for EC towers based on the description of tower footprints from site PIs.

We evaluated the TROPOMI SIF_{dc} data against a tower-based SIF product in CA-Obs (Pierrat *et al* 2022, Pierrat and Stutz 2022), which is close to our study area but outside the LC map. A 2D scanning telescope measures SIF at 745–758 nm across a canopy representative loop that repeats every half hour, from which we calculated daily mean SIF at eight-day intervals. The International Geosphere-Biosphere Programme (IGBP) classification of CA-Obs is evergreen needleleaf forests (ENF). Thus, we used it to

benchmark FluxCom GPP and gridded TROPOMI SIF_{dc} in *Evergreen forest*.

3. Results

3.1. Annualized relationship of SIF and GPP

The 95th percentiles of TROPOMI SIF_{dc} and snow-free FluxCom GPP are not consistent across space (figures 1(c) and (d)), suggesting that the regression slope k is not homogeneous in the Arctic-Boreal region. *Tussock Tundra* on the North Slope of the Brooks Range has a higher 95th percentile of SIF_{dc} than the surrounding area, while the 95th percentile of GPP is similar to the surrounding area. The 95th percentile of SIF_{dc} is high in the southern portion of our study area, which may be attributed to agricultural land located in southern Alberta and Saskatchewan (Guanter *et al* 2014).

The dynamic ranges of GPP and SIF_{dc} vary with land covers (figure 2). The growing season maximal GPP is lowest in land covers with lower statures, such as *Low Shrub* and *Tussock Tundra*. The growing season maximal SIF_{dc} is often lower than 0.5 mW m⁻² sr⁻¹ nm⁻¹ except in *Deciduous Forest*, *Woodland*, *Tall Shrub*, and *Herbaceous*.

In *Woodland*, the linear SIF $_{\rm dc}$ -GPP relationship splits (figure 2(d)) because *Woodland* is a heterogeneous land cover type coexisting with other land covers (Wang *et al* 2019). Thus, the SIF $_{\rm dc}$ -GPP relationship of *Woodland* contains the features of both high- and low-statured land cover types.

The linear correlation of GPP and SIF_{dc} from gridded products is comparable to tower-based measurements (figure 2). Except for *Evergreen Forest* and *Fen*, where the maximum EC GPP is lower than FluxCom GPP, FluxCom GPP may be overestimated. EC GPP can be negative during winter, which is an artifact of the flux partitioning (Hagen *et al* 2006, Wutzler *et al* 2018). The daily mean SIF from the tower-based instrument in CA-Obs nicely falls in the dynamic range of TROPOMI SIF_{dc} (figures 2(a) and C.7).

On average, the highest regression slope k among the vegetation dominated land cover types occurs in *Evergreen forest* (33.84 (gC m⁻² day⁻¹)/ (mW m⁻² sr⁻¹ nm⁻¹)), while the lowest k value is in *Tussock Tundra* (12.89 (g Cm⁻² day⁻¹)/ (mW m⁻² sr⁻¹ nm⁻¹)).

3.2. Spatial patterns of the SIF-GPP relationship

The spatial distribution of the resulting regression slope *k* (figure 3(a)) is primarily a function of land cover types (figure 1(a)). Similar to figure 2, *k* is higher in *Evergreen forest*, which is in the southwest part of the study area, and lower in *Tussock Tundra* on the North Slope of the Brooks Range.

The correlation between SIF and GPP (Pearson's r^2 ; figure 3(b)) depends on the synchrony of the seasonal trajectories of SIF_{dc} and GPP. Most of our study

Table 1. EC towers with GPP data used in this study. LC30M is the land cover type based on the original spatial resolution $(30 \text{ m} \times 30 \text{ m})$ of Wang et al (2019). LC008333D is the dominant land cover type in the resolution of

Name	LC30M	LC008333D	IGBP	Tower footprint LC	Mean canopy height (m)	Elevation (m)	Start month	End month	Reference
CA-HPC	Fen	Woodland	ENF	Woodland	3.93	08	April 2017	November 2017	Sonnentag and Marsh
CA-Obs	I	I	ENF	Evergreen Forest	14	629	July 2019	December 2020	(2021a) Black (2016), Pierrat and
CA-SMC	Woodland	Water	ENF	Evergreen Forest	6.15	150	July 2017	November 2017	Sonnentag (2021)
CA-TVC	Herbaceous	Low Shrub	HSO	Low Shrub	0.25	85	May 2017	October 2017	Sonnentag and Marsh
									(2021b)
DEJU	Evergreen Forest	Woodland	ENF	Evergreen Forest	10	529	January 2018	September 2021	NEON (2022)
US-An1	Sparsely Vegetated	Tussock Tundra	HSO	Sparsely Vegetated	9.0	009	June 2017	August 2017	Rocha <i>et al</i> (2016b)
US-An3	Tussock Tundra	Tussock Tundra	HSO	Tussock Tundra	0.2	009	June 2017	August 2017	Rocha et al (2016a)
US-Atq	Low Shrub	Sparsely Vegetated	WET	Tussock Tundra	0.12	15	January 2017	December 2017	Oechel <i>et al</i> (2014)
US-BZB	Woodland	Deciduous Forest	WET	Fen	1	100	January 2017	December 2017	Euskirchen (2021a)
US-BZF	Low Shrub	Deciduous Forest	WET	Fen	1	95	January 2017	December 2017	Euskirchen (2021b)
US-BZS	Woodland	Deciduous Forest	ENF	Evergreen Forest	2.5	100	January 2017	December 2017	Euskirchen (2021c)
US-ICh	Low Shrub	Tussock Tundra	HSO	Low Shrub	0.1	940	January 2017	December 2017	Euskirchen et al (2016a)
US-ICs	Tussock Tundra	Tussock Tundra	WET	Fen	0.1	920	January 2017	December 2017	Euskirchen et al (2016b)
US-ICt	Tussock Tundra	Tussock Tundra	HSO	Tussock Tundra	0.1	930	January 2017	December 2017	Euskirchen et al (2016c)
US-Ivo	Herbaceous	Low Shrub	WET	Tussock Tundra	0.1	268	January 2004	December 2007	Zona and Oechel (2016)
US-Prr	Woodland	Woodland	ENF	Evergreen Forest	2.9	210	January 2017	October 2017	Kobayashi et al (2016)

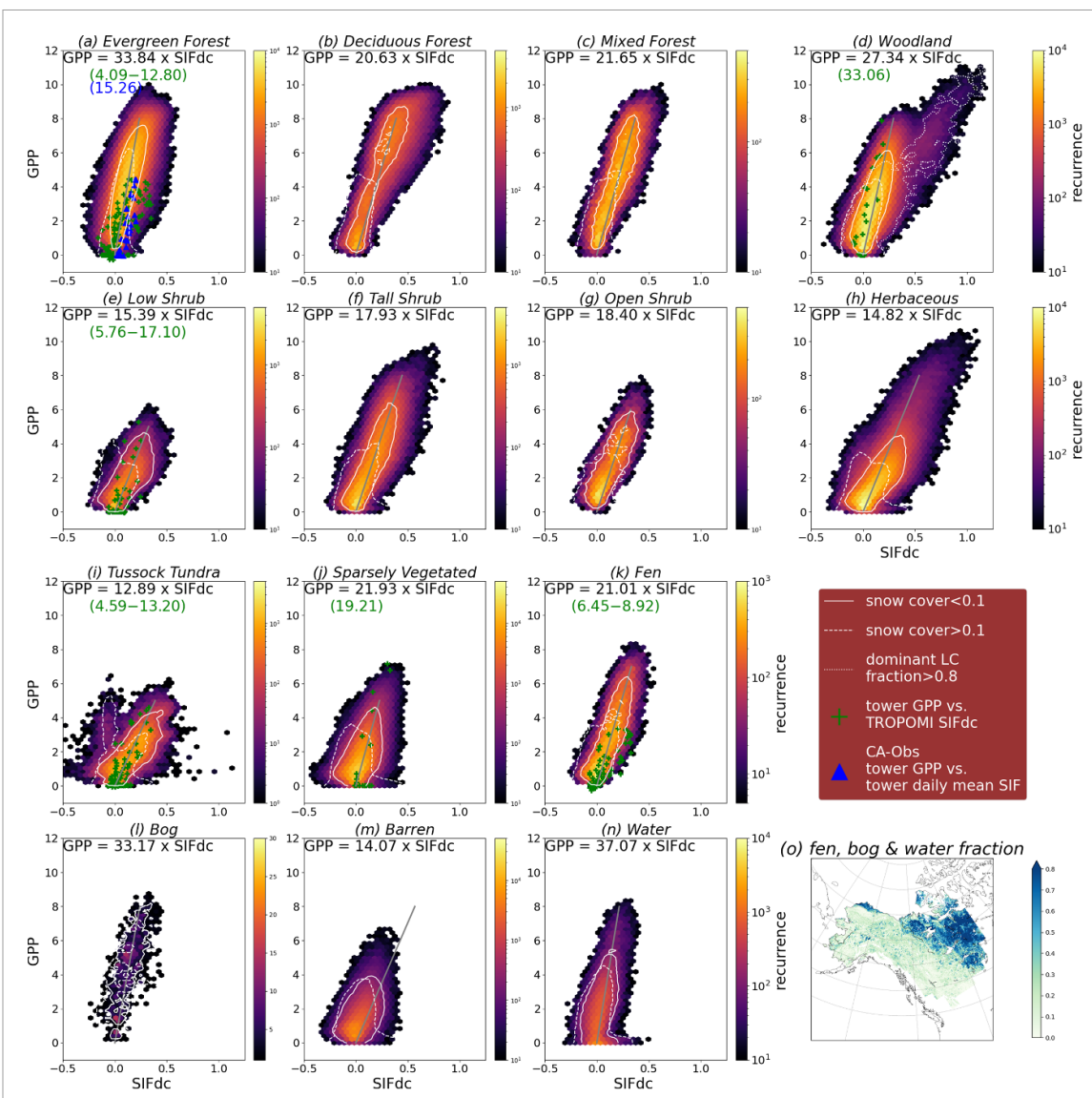


Figure 2. The hexbins are pixels categorized by the dominant land cover types in figure 1(a) based on all data of 2018–2019 eight-day TROPOMI SIF_{dc} (mW m⁻² sr⁻¹ nm⁻¹) and FluxCom GPP (gC m⁻² day⁻¹) in the study area. The color of hexbins represents the pixel recurrence at a given pair of SIF_{dc} and GPP bins. The white solid contours are the 95 percentile of the recurrence when the snow cover is less than 0.1 (snow-free). The white dashed contours are the 95 percentile of the recurrence when the snow cover is greater than 0.1. The dotted white contour in (d) is the 95 percentile of grids where the dominant land cover (a.k.a Woodland) fraction is greater than 80%. The gray line is the mean SIF-GPP relationship with the math expression noted in each land cover type. The blue triangles are the multi-year average of eight-day tower-based daily mean EC GPP from CA-Obs, whose regression slope *k* is written in blue. The green crosses are the multi-year average of eight-day TROPOMI SIF_{dc} and daily mean EC GPP from all other EC towers according to land cover types. The range of regression slopes of green crosses from different towers is written in green. Panel (o) shows the area fraction occupied by *Fen*, *Bog*, and *Water*.

area has moderate to high Pearson's r^2 (figure 3(b)), where SIF_{dc} and GPP peak simultaneously across our study area (figures 1(e) and (f)).

In the *Sparsely vegetated* northeastern part of the study area, Pearson's r^2 is low, and the annual mean EI (figure 3(f)) is high, indicating that the FluxCom models predict GPP in this region with few training samples and thus yield higher uncertainties. The high seasonal range in EI (figure 3(d)) suggests the extrapolation is more severe in winter than in summer.

The reduced χ^2 is much higher than 1 near glacial lakes in Northern Canada (figure 3(a)) and *Deciduous forest*, indicating the empirically fitted SIF-GPP relationship is underestimated and does not fully

capture the seasonal trajectories in SIF_{dc} and GPP. One possible reason is that most training samples used by FluxCom models in the Arctic-Boreal are not *Deciduous forest* (figures 1(a) and 3(f)). Thus, the FluxCom models have to extrapolate from training samples that are less similar to the environment of the region so that the FluxCom GPP has a higher error in *Deciduous* forest.

3.3. Overestimated FluxCom GPP in wetlands

Similar to other reflectance-based GPP products (Joiner *et al* 2018), we found FluxCom GPP may be overestimated in wetlands. In *Fen*, FluxCom GPP is substantially higher than EC GPP (figure 2(k))

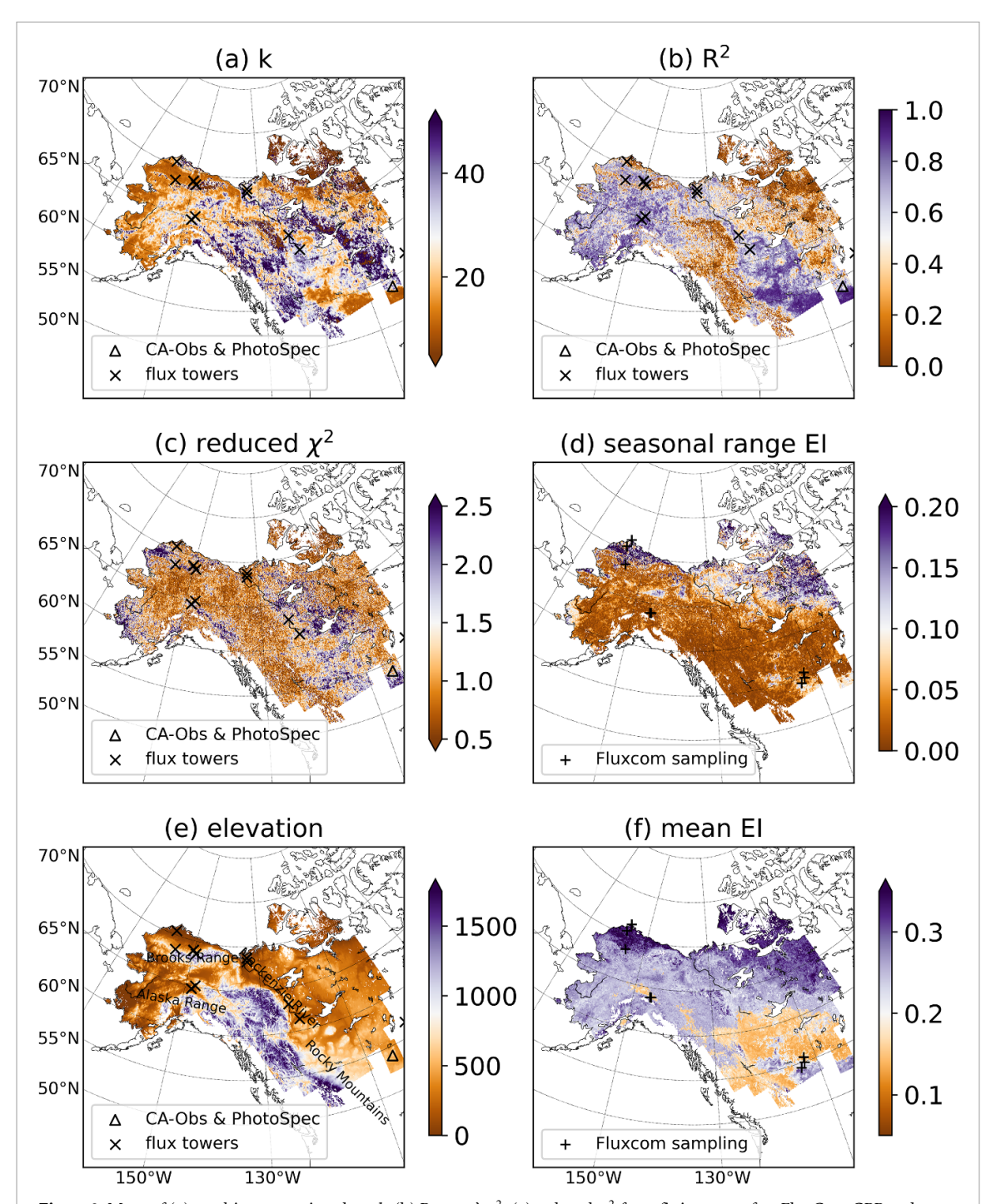


Figure 3. Maps of (a) resulting regression slope k, (b) Pearson's r^2 , (c) reduced χ^2 from fitting snow-free FluxCom GPP and TROPOMI SIF_{dc}. Panel (e) is the elevation map of the study region. The scatters in (a)–(c) and (e) are the EC towers with ground-level GPP data and/or SIF measurements, which are used in figure 2. Panels (d) and (f) are the multi-year average of the seasonal range (winter (January and February)–summer (June and July)) and the annual mean of Extrapolation Index (EI) from Jung $et\ al\ (2020)$. The scatters in (d) and (f) are the EC towers used to train FluxCom models. The maps are extended to the area surrounding CA-Obs since data are available.

and other non-wetland herbaceous land cover types (figure 2). In *Bog* and *Water*, FluxCom GPP is also unrealistically high while SIF_{dc} is around 0. These results suggest a potential overestimation of FluxCom GPP in wetlands.

This bias caused by water is more significant in the area with a high fraction of wetlands (figure 2(0)), where the annual mean and seasonal range of EI are also high (figures 3(d) and (f)).

3.4. Topographic impact on the SIF-GPP relationship

There is a topographic dependence of k and Pearson's r^2 . k (Pearson's r^2) is higher (lower) along the Brooks Range, the Mackenzie River, the Alaska Range, and the north end of the Rocky Mountains (figures 3(a)–(c) and (e)). Meanwhile, the reduced χ^2 is mostly around 1 across topography, suggesting the fitted SIF-GPP relationship is reliable.

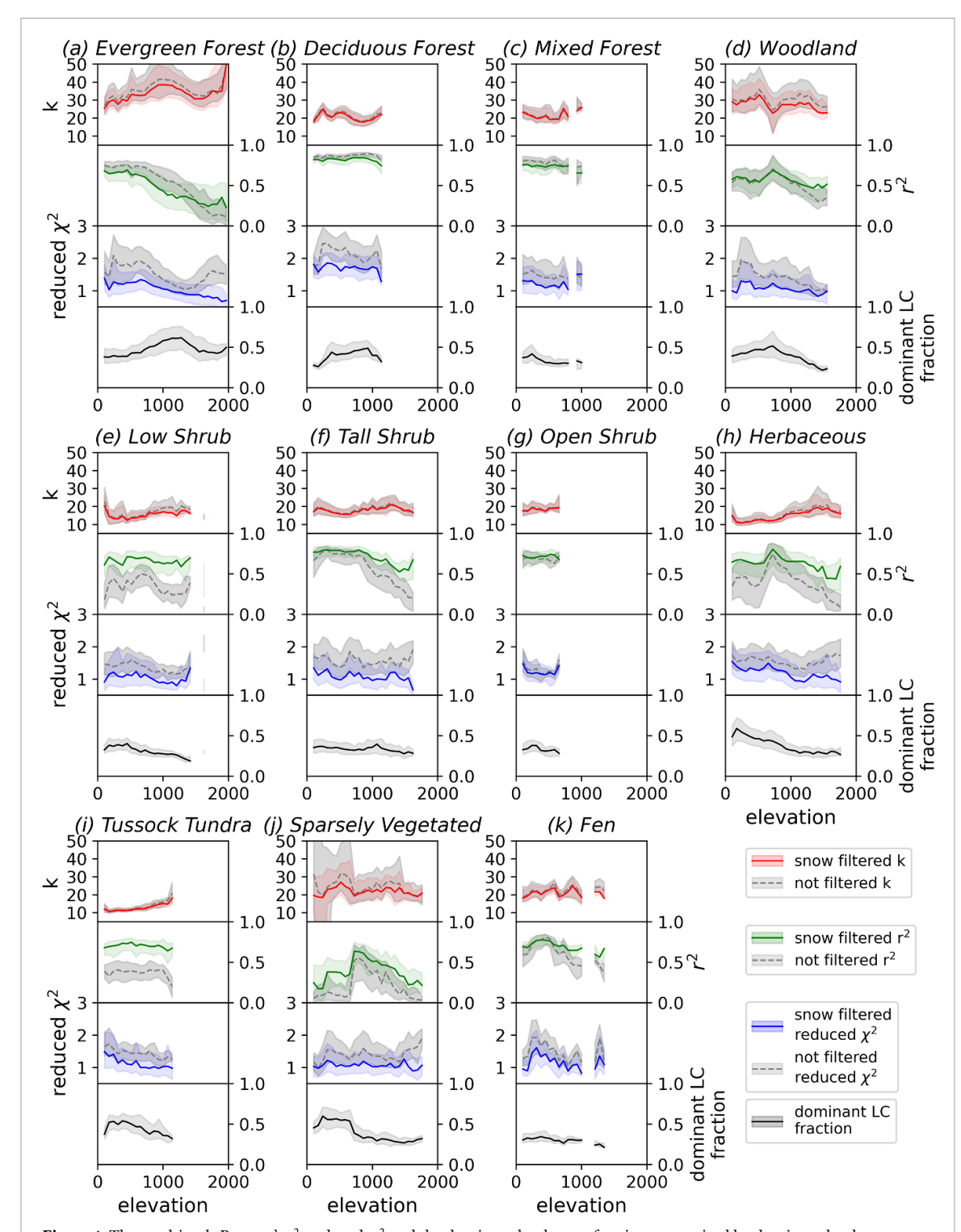


Figure 4. The resulting k, Pearson's r^2 , reduced χ^2 and the dominant land cover fraction categorized by dominant land cover types as a function of surface elevation. The color lines are the results from snow-free data (snow cover is less than 0.1). The gray dashed lines are the results from snow-contaminated data (snow cover is greater than 0.1). The shades are the interquartile range of the results from all grid-time in each dominant land cover type. *Bog* has too few grids to show the dependence on elevation. *Barren* and *Water* land cover types are omitted since they are not vegetation dominated.

The resulting k of Evergreen Forest shows a strong dependence on elevation as the dominant land cover fraction varies (figure 4(a), Funk et al 2004, Roland et al 2021). For example, when Evergreen forest becomes more abundant, k is higher between 1000 and 1500 m in elevation. Above the

tree line (\sim 1500 m), k drops as the fraction of grid composed of *Evergreen forest* reduces. The highest k in *Evergreen forest* is obtained at a 2000 m elevation which can be noisy because the reduced χ^2 is much less than 1 suggesting the linear model overfits the data.

3.5. Snow contamination and snow impact on the SIF-GPP relationship

FluxCom GPP is occasionally unrealistically high during winters, when SIF_{dc} is around zero (figure 2). We found that this is a sign of snow contamination, especially in the land cover types with lower canopy heights, such as *Low shrub*, *Herbaceous*, and *Tussock Tundra* (figures 2(e), (h) and (i)). After snowy pixels were filtered, the distribution of TROPOMI SIF_{dc} and FluxCom GPP is more towards linear.

Although the change in resulting k due to snow filtering is small, snow filtering has substantially improved the goodness of fit by increasing Pearson's r^2 and/or pushing the reduced χ^2 towards 1 (figure B.6) across all land cover types and all elevations, especially in low-statured land covers, such as *Low shrub*, *Herbaceous*, and *Tussock Tundra* (figures 4(e), (h) and (i)) where the split distribution pattern due to snow contamination is observed in figure 4. In forests (figures 4(a)–(c)), although Pearson's r^2 decreases, the reduced χ^2 has been improved by approaching 1.

4. Discussion

4.1. Opportunities for remotely evaluating GPP seasonality in the Arctic-Boreal region

We reported and evaluated the SIF-GPP relationship in the context of Arctic-Boreal land cover types at the regional scale. The extensive spatial coverage of our study and validation from EC GPP and towerbased SIF data underscores the potential of using remote sensing and machine learning techniques in the Arctic-Boreal region if remote sensing data are carefully filtered for snow contamination.

Benefiting from the extensive spatial coverage, FluxCom GPP and TROPOMI SIF fill the gaps in land cover types that are too remote to be extensively sampled by ground-based measurements (Virkkala *et al* 2022) or in complex terrain where eddy-covariance techniques are challenging to apply (Paw U *et al* 2000, Baldocchi 2003).

4.2. Uncertainties in the SIF-GPP relationship in the Arctic-Boreal region

Contrasting to a universal k for all land cover types solved in Sun et al (2017), Li et al (2018), and Li and Xiao (2022), we found it is challenging to find a one-model-fits-all approach to estimate GPP using SIF_{dc} in the Arctic-Boreal region, especially across multiple land cover types or even within the same dominant land cover types. The heterogeneous land cover and complex terrain in the Arctic-Boreal region further complicate interpreting the fitted SIF-GPP relationship and resulting k values. The elevational and spatial gradients of sub-pixel land cover contribute to the uncertainties of k among the pixels of the same dominant land cover types. For future studies, comprehensive sampling of the physiological traits

(such as LUE, Φ_F , and $f_{\rm esc}$; equation (4)) across land covers can help mechanistically explain the variations in k.

Another source of uncertainties in the SIF-GPP relationship is the temporal variability due to seasonally biased sampling of remotely sensed SIF and GPP. Because both TROPOMI SIF and MODIS data used in FluxCom GPP are derived from optical measurements, the large seasonal fluctuations of the solar radiation in the Arctic-Boreal regions lead to seasonal variabilities of valid soundings (Cheng *et al* 2022) and uncertainties. Our study provided both Pearson's r^2 and reduced χ^2 to help biosphere modelers use the resulting k judiciously considering the uncertainty of both SIF and GPP as well as the linearity between SIF and GPP.

The asynchrony of SIF and GPP can also deteriorate the linearity of SIF-GPP relationship. Because SIF contains the information of both APAR and LUE, the seasonal trajectory of SIF may deviate from the reflectance/APAR-based GPP products (such as Flux-Com GPP) (Walther *et al* 2016, 2018, Maguire *et al* 2021). Long-term and continuous EC GPP can help better constrain the temporal uncertainty in remote sensing-based GPP products.

It is worth noting that complex terrain may cause high uncertainties in TROPOMI measurements (Turner *et al* 2020) and inaccurate length-of-day correction factors in SIF $_{\rm dc}$ (Cheng *et al* 2022, Köhler *et al* 2018), leading to larger uncertainties in the SIF-GPP relationship. Fortunately, these impacts are negligible in this study since there are no missing samples due to topography (figure A.5), and the footprint of TRO-POMI soundings (5 km \times 3.5 km at nadir, or up to 14 km at the edges of the swath) are large enough to average out the topographic impact on the length-of-day correction factor (Cheng *et al* 2022).

4.3. Variability of k values across latitudes and data products

Due to the non-uniform spectral shape of SIF, our k values are only suitable for estimating GPP with SIF measurements at 740 nm and not comparable to the k values evaluated by SIF at different wavelengths (Guanter *et al* 2012, Sun *et al* 2017, Li *et al* 2018, Zhang *et al* 2020).

Compared to the studies using the same TRO-POMI SIF (Turner *et al* 2021, Li and Xiao 2022, Liu *et al* 2022), our study yields much higher *k* values, especially in high-statured land cover types. Since those previous studies (Turner *et al* 2021, Li and Xiao 2022, Liu *et al* 2022) mostly focus on lower latitudes, the disagreement in *k* of the same land cover types may indicate different vegetation composition, photosynthetic productivity, fluorescence yield, sub-pixel variability, and/or canopy openness across latitudes (Prock and Körner 1996, Kreyling 2020, Crous *et al* 2022) as suggested in equation (4).

The different k across spatial scales (figures 2 and C.7) and between our results and previous studies (Turner *et al* 2021, Li and Xiao 2022, Liu *et al* 2022) can also be attributed to the inconsistency between FluxCom and EC GPP (Sun *et al* 2017). Next, we will discuss the potential biases in Fluxcom GPP.

4.4. Limitations in FluxCom GPP

4.4.1. Snow contamination

Although the original FluxCom GPP product has already removed some snowy pixels by using MODIS quality flags (Jung *et al* 2020), we found some snow contamination still exists (figure 2). In this study, we used a more conservative snow filter (<0.1) to showcase the snow contamination in FluxCom GPP propagated from remote sensing products (Jin *et al* 2017, Myers-Smith *et al* 2020). More importantly, our results suggest that quantitative and standalone information on snow coverage in addition to quality flags is helpful for improving future machine learning products (Chen *et al* 2018).

Snow contamination does not impact all land cover types equally. Low-statured land cover types are more likely to have unrealistically high FluxCom GPP before the growing season starts (figure 2). Thus, the universal snow filter we used in this study may be too conservative. For future studies, rigorous validation of snow measurements at regional scales will greatly improve canopy radiative transfer simulations and optical remote sensing retrievals at the Arctic-Boreal region (Kobayashi *et al* 2007, Kobayashi and Iwabuchi 2008, Chen *et al* 2018).

4.4.2. Underrepresented water

Contrary to attributing the high k values in wetlands to underestimated SIF (Chen *et al* 2021), our results suggest the unrealistically high FluxCom GPP is the reason for high k values in wetland land cover types. FluxCom GPP has been overestimated because NDVI of surface water in mixed pixels with both vegetation and surface water is understated (Jiang *et al* 2005, 2006, Huemmrich *et al* 2021). Using near-infrared reflectance of vegetation for FluxCom models may better account for the dark surface water reflectance than NDVI and improve the SIF-GPP relationship (Badgley *et al* 2019).

This bias further compounds the uncertainty due to a lack of sampling as high EI and high wetland area fractions collocate. Taken together, these two issues can limit the application of FluxCom GPP in the Arctic-Boreal region (figure 2(o); Stow *et al* 2004, Muster *et al* 2013).

4.4.3. Extrapolation of training data

Because the spread in FluxCom GPP ensembles may not fully represent the disagreement between Flux-Com and EC GPP when there are few EC towers as training samples for FluxCom (Pallandt *et al* 2022), the resulting *k* values may be more reliable where

FluxCom and EC GPP are similar (such as *Tussock Tundra* and *Low Shrub*; figures 2(e) and (i)) than the ones where the FluxCom GPP is substantially overestimated (such as *Evergreen forest* and *Fen*; figures 2(a) and (k)).

Nevertheless, there is a time mismatch between FluxCom GPP and EC GPP (table 1) in this study, where the inter-annual variability of GPP seasonality is ignored. In future studies, more active EC towers with long-term record of GPP are needed to improve FluxCom GPP.

4.5. Limitations from heterogeneous sub-pixel land cover

We showed that land cover in the Arctic-Boreal region is highly heterogeneous at sub-pixel. The dominant vegetated land cover types on average occupy less than 50% of the area in each $0.08333^{\circ} \times 0.08333^{\circ}$ grid (figure 1(b)). Because heterogeneous land cover can blur the distinct SIF-GPP relationship of each individual land cover type (Zhang et al 2020), it is challenging to unmix the contribution of subpixel land cover types at the current spatial scale. This results in a few notable limitations in our study: (a) The land cover definitions of EC towers are different according to 30 m vicinity (LC30M), 0.083 33° vicinity (LC008333D), and the actual footprint of towers based on PI's descriptions (tower footprint land cover in table 1). The observed vegetation composition and determining factor (physiology vs light absorption) for SIF variability may also shift across spatial scales (Maguire et al 2021), even though the dynamic range of SIF_{dc} amplitude in our study is consistent from ground level to satellite level (figure C.7). As a result, there may be a mismatch of land cover types when we benchmark across spatial scales. (b) As discussed in section 4.4.2, the presence of surface water contributes to the sub-pixel variations in other dominant land cover types and adds to the ambiguity of our results (Myers-Smith et al 2020). (c) The land cover definition used here does not consider agricultural land cover, which is not negligible in southern Alberta and Saskatchewan (Guanter et al 2014) and yields a different SIF-GPP relationship than the non-agriculture land cover types. And (d) Given the rapid changes in the Arctic-Boreal region (Hobbie et al 2017, Box et al 2019, Wang et al 2020, Canadell et al 2021, Curasi et al 2022), our land cover information from 2014 (Wang et al 2019) can be outdated, which will impact our definition of dominant land cover types and the classification of results.

5. Conclusions

In this study, we evaluated the empirical linear relationship of SIF_{dc} and GPP across the Arctic-Boreal region from the perspectives of Pearson's r^2 and the

goodness of fit. Our results show the promise of monitoring Arctic-Boreal vegetation using novel remote sensing tools after careful quality control. For the first time, our study reports the fitted regression slope k as well as the uncertainties of fitted SIF_{dc}-GPP relationship for the land cover types that are unique to the Arctic-Boreal region. The resulting k, Pearson's r^2 , and reduced χ^2 together can help biosphere modelers improve the estimation of GPP in the Arctic-Boreal regions and cope with model-data uncertainties.

Data availability statement

The data that support the findings of this study are openly available at the following URL/DOI: https://data.caltech.edu/records/20216.

Acknowledgments

This research is supported by the NASA ABoVE (Award 80NSSC19M0129) and OCO Science team projects (Award 80NSSC18K0895). This material is also based upon work supported by the National Science Foundation Graduate Research Fellowship under Grant Nos. DGE-1650604 and DGE-2034835. Funding for US-BZB, US-BZF, US-BZS, US-ICh, US-ICs, and US-ICt was provided by the US Geological Survey, Research Work Order 224 to the University of Alaska Fairbanks, the Bonanza

Creek Long-Term Ecological Research Program funded by the National Science Foundation (NSF DEB-1026415, DEB-1636476), the NSF Long-Term Research in Environmental Biology Program (NSF LTREB 2011276), and the NSF Arctic Observatory Network Program (NSF 1936752, 1503912, and 110789). Oliver Sonnentag acknowledges funding by the Canada Research Chairs, Canada Foundation for Innovation Leaders Opportunity Fund, and Natural Sciences and Engineering Research Council Discovery Grant programs. Sophia Walther acknowledges support from ESA within the Living Planet Fellowship project 'Vad3e mecum'. We use a Julia gridding package from https://github.com/cfranken/gridding.

Appendix A. Gridding TROPOMI SIF

We gridded individual soundings into an eight-day temporal resolution and a spatial resolution of $0.0833^{\circ} \times 0.0833^{\circ}$. The soundings were filtered with cloud fractions smaller than 0.8, which also includes additional retrieval quality filter criteria and is the suggested standard filter for public use of SIF data (Köhler *et al* 2018). Even though the viewing geometry of individual sounding varies, the effect viewing geometry over the eight-day period can be negligible. On average, there are more than five soundings falling in each $0.0833^{\circ} \times 0.0833^{\circ}$ grid cell in our study region (figure A.5).

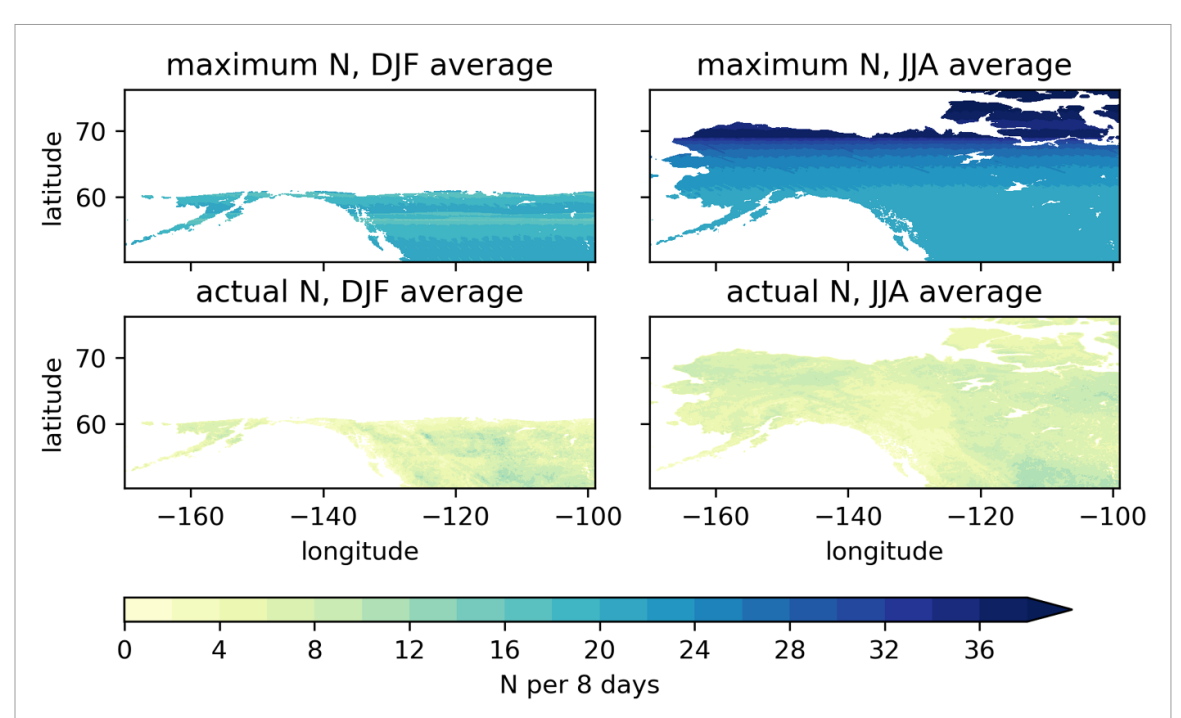


Figure A.5. In the study area (core region of the Arctic-Boreal vulnerability experiment (ABoVE) domain) and the resolution of eight days, in each 0.083 33° × 0.083 33° grid in 2020: (a) the December, January, and February (DJF) average of maximum (total) number of soundings; (b) the June, July, and August (JJA) average of maximum (total) number of soundings; (c) the DJF average of actual (filtered) number of soundings; and (d) the JJA average of actual (filtered) number of soundings.

Appendix B. Snow filters

We also tested different snow covers as thresholds. We found the snow filter works well for removing snow-contaminated FluxCom GPP and improving the goodness of the fit of the SIF-GPP relationship. For example, US-ICt, a *Tussock Tundra* site, represents the lower-stature canopies

that benefit from the snow filter. Snow filters remove snow-contaminated FluxCom GPP during the growth onset, which has a higher error bar. In this example, a strict snow filter (a smaller value of snow cover) includes fewer data for the regression but improves the goodness of the fit by increasing Pearson's r^2 and pushing the reduced χ^2 towards 1.

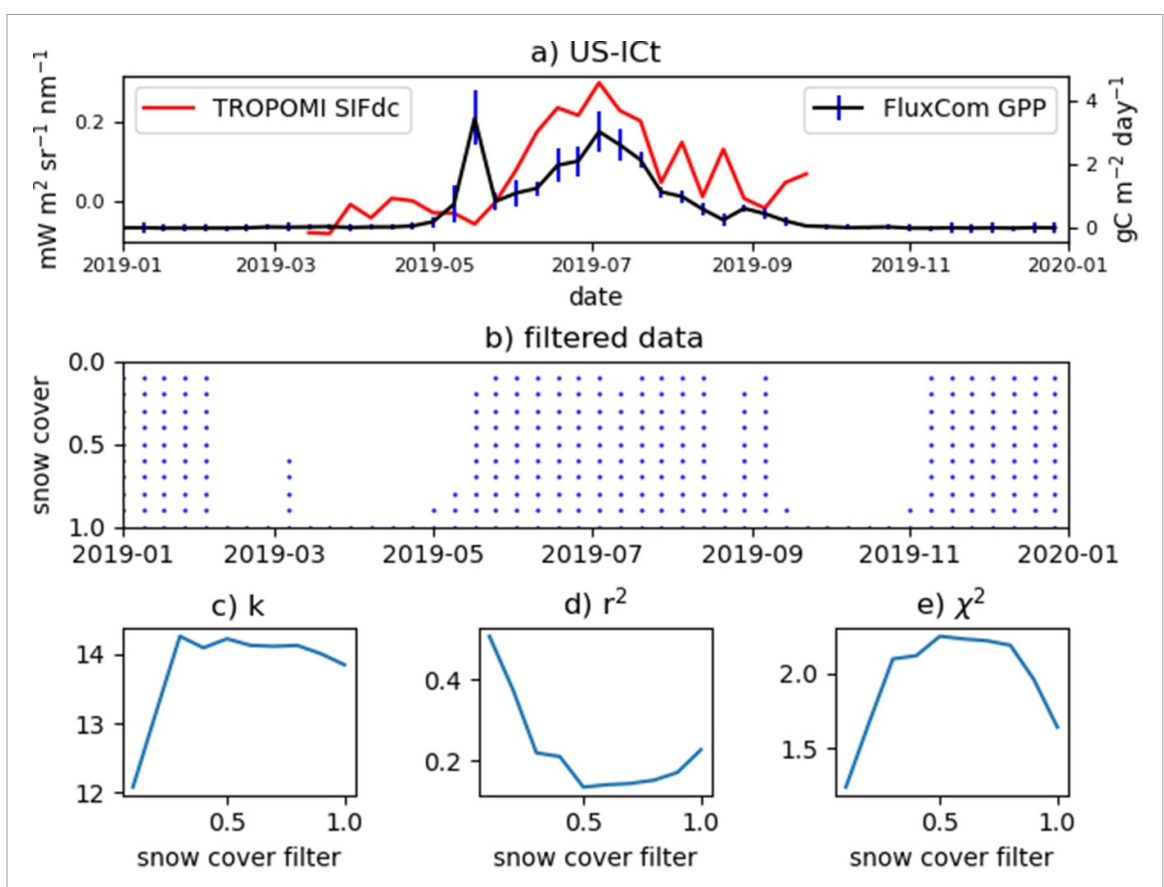


Figure B.6. (a) Time series of TROPOMI SIF_{dc} and FluxCom GPP at Imnavait Creek Watershed Tussock Tundra site (US-ICt) in 2019. (b) The filtered data (blue dots) based on snow covers (MOD10C2). (c)–(e) The resulting k, Pearson's r^2 , and reduced χ^2 as a function of snow filter (snow cover).

Appendix C. Spatial upscaling

For CA-Obs, where we have observations (climatology) of SIF_{dc} and GPP at both tower and gridded scales, we compared the measurements across spatial scales (figure C.7). The seasonality and magnitude of SIF_{dc} across spatial scales are mostly consistent,

while FluxCom GPP and EC GPP are not consistent and entirely synchronized. The difference in both the amplitude and timing of seasons between the two SIF products may be attributed to the deciduous trees and understory, which are more visible from space (TRO-POMI) than the tower instrument (PhotoSpec) due to the shallower view angles of PhotoSpec.

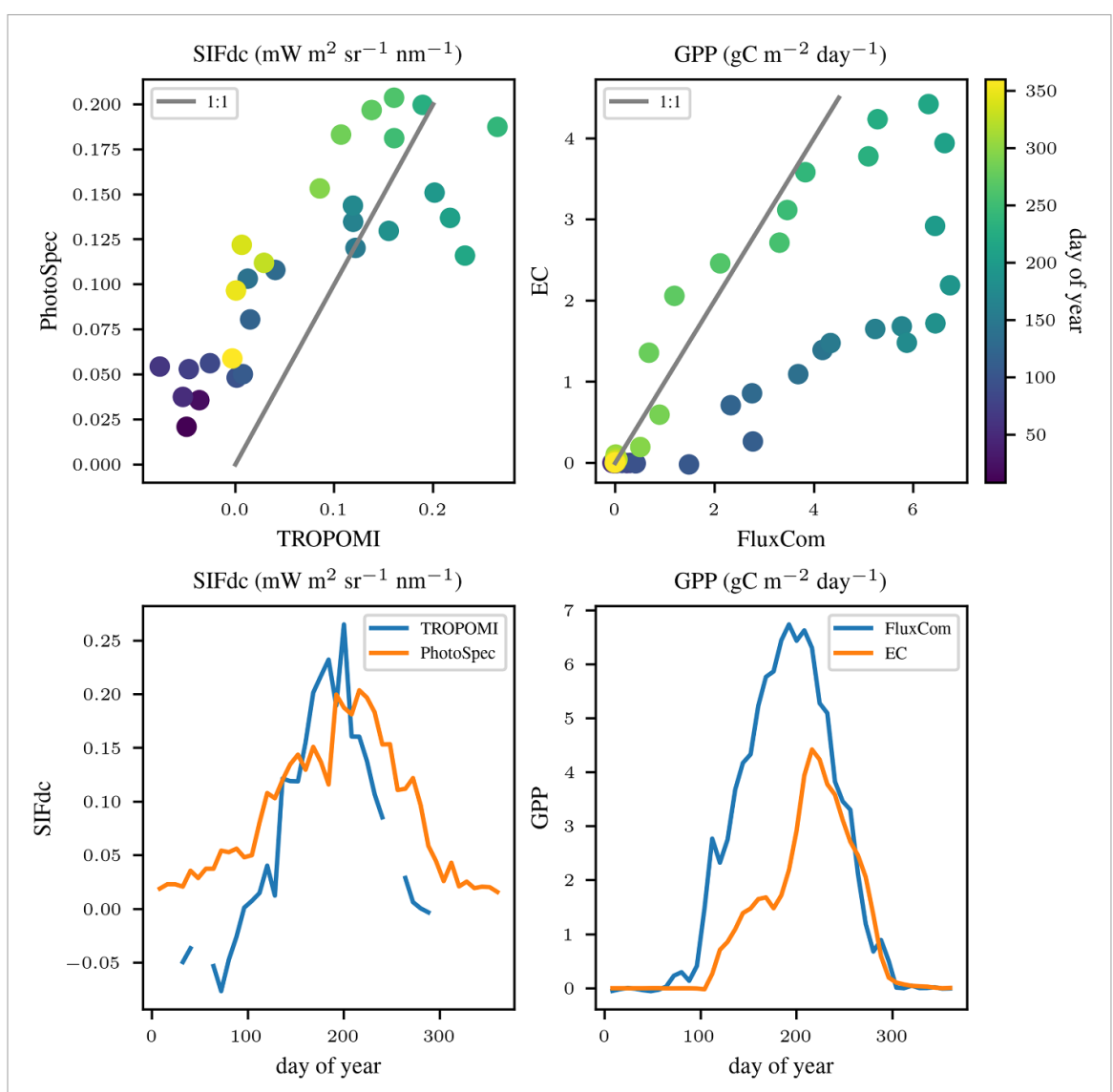


Figure C.7. In CA-Obs, comparing the climatology of SIF $_{dc}$ and GPP across spatial scales. (a) TROPOMI SIF $_{dc}$ vs PhotoSpec daily mean SIF (b) FluxCom GPP vs EC GPP. (c) Timeseries of TROPOMI SIF $_{dc}$ and PhotoSpec daily mean SIF. (d) Timeseries of FluxCom GPP and EC GPP. The climatology of TROPOMI SIF $_{dc}$ and FluxCom GPP is averaged from 2018 to 2019. The climatology of PhotoSpec daily mean SIF and EC GPP is averaged from July 2019 to December 2020.

ORCID iDs

Rui Cheng https://orcid.org/0000-0002-3003-8339

Zoe Pierrat https://orcid.org/0000-0002-6726-2406

Philipp Köhler https://orcid.org/0000-0002-7820-

Adrian V Rocha 6 https://orcid.org/0000-0002-4618-2407

References

Badgley G, Anderegg L D L, Berry J A and Field C B 2019 Terrestrial gross primary production: using NIR $_{
m V}$ to scale from site to globe Glob. Change Biol. 25 3731–40

Baldocchi D D 2003 Assessing the eddy covariance technique for evaluating carbon dioxide exchange rates of ecosystems: past, present and future *Glob. Change Biol.* **9** 479–92 Beer C *et al* 2010 Terrestrial gross carbon dioxide uptake: global distribution and covariation with climate *Science* 329 1184984

Black T A 2016 FLUXNET2015 CA-Obs Saskatchewan-Western Boreal, mature Black spruce (https://doi.org/10.18140/FLX/ 1440044)

Boggs P T and Rogers J E 1989 Orthogonal Distance Regression in Statistical analysis of measurement error models and applications: proceedings of the AMS-IMS-SIAM joint summer research conference *Contemporary Mathematics* vol 112 p 186

Bowling D R, Logan B A, Hufkens K, Aubrecht D M,
Richardson A D, Burns S P, Anderegg W R L, Blanken P D
and Eiriksson D P 2018 Limitations to winter and spring
photosynthesis of a Rocky Mountain subalpine forest *Agric.*For. Meteorol. 252 241–55

Box J E et al 2019 Key indicators of Arctic climate change: 1971–2017 Environ. Res. Lett. 14 045010

Bruun H H, Moen J, Virtanen R, Grytnes J-A, Oksanen L and Angerbjörn A 2006 Effects of altitude and topography on species richness of vascular plants, bryophytes and lichens in Alpine communities *J. Veg. Sci.* 17 37–46

Canadell J G, Monteiro P M S and Costa M H 2021 Global Carbon and other Biogeochemical Cycles and Feedbacks

- Climate Change 5 2021: The Physical Science Basis.
 Contribution of Working Group I to the Sixth Assessment
 Report of the 6 Intergovernmental Panel on Climate Change
 (Cambridge: Cambridge University Press) (https://doi.org/10.1017/9781009157896.007)
- Chen A, Mao J, Ricciuto D, Lu D, Xiao J, Li X, Thornton P E and Knapp A K 2021 Seasonal changes in GPP/SIF ratios and their climatic determinants across the Northern Hemisphere Glob. Change Biol. 27 5186–97
- Chen N, Li W, Gatebe C, Tanikawa T, Hori M, Shimada R, Aoki T and Stamnes K 2018 New neural network cloud mask algorithm based on radiative transfer simulations *Remote Sens. Environ.* **219** 62–71
- Cheng R *et al* 2020 Decomposing reflectance spectra to track gross primary production in a subalpine evergreen forest *Biogeosciences* 17 4523–44
- Cheng R, Köhler P and Frankenberg C 2022 Impact of radiation variations on temporal upscaling of instantaneous solar-induced chlorophyll fluorescence *Agric. For. Meteorol.* **327** 109197
- Cihlar J 1996 Identification of contaminated pixels in AVHRR composite images for studies of land biosphere *Remote Sens*. *Environ.* **56** 149–63
- Crous K Y, Uddling J and De Kauwe M G 2022 Temperature responses of photosynthesis and respiration in evergreen trees from Boreal to tropical latitudes *New Phytol*. 234 353–74
- Curasi S R *et al* 2022 Range shifts in a foundation sedge potentially induce large Arctic ecosystem carbon losses and gains *Environ. Res. Lett.* 17 045024
- Delaria E R, Place B K, Turner A J, Zhu Q, Jin X and Cohen R C 2021 Development of a solar-induced fluorescence—canopy conductance model and its application to stomatal reactive nitrogen deposition ACS Earth Space Chem. 5 3414—28
- Dobrowski S Z 2011 A climatic basis for microrefugia: the influence of terrain on climate *Glob. Change Biol.* 17 1022–35
- Earth Resources Observation And Science (EROS) Center 2017 Global 30 Arc-second elevation (GTOPO30) (https://doi. org/10.5066/F7DF6PQS)
- Euskirchen E 2021a AmeriFlux AmeriFlux US-BZB Bonanza Creek Thermokarst Bog (https://doi.org/10.17190/AMF/ 1773401)
- Euskirchen E 2021b AmeriFlux AmeriFlux US-BZF Bonanza Creek Rich Fen (https://doi.org/10.17190/AMF/1756433)
- Euskirchen E 2021c AmeriFlux AmeriFlux US-BZS Bonanza Creek Black spruce (https://doi.org/10.17190/AMF/ 1756434)
- Euskirchen E, Shaver G and Bret-Harte S 2016a AmeriFlux AmeriFlux US-ICh Imnavait Creek watershed heath tundra (https://doi.org/10.17190/AMF/1246133)
- Euskirchen E, Shaver G and Bret-Harte S 2016b AmeriFlux AmeriFlux US-ICs Imnavait Creek watershed wet sedge tundra (https://doi.org/10.17190/AMF/1246130)
- Euskirchen E, Shaver G and Bret-Harte S 2016c AmeriFlux AmeriFlux US-ICt Imnavait Creek watershed Tussock tundra (https://doi.org/10.17190/AMF/1246131)
- Fisher J B *et al* 2014 Carbon cycle uncertainty in the Alaskan Arctic *Biogeosciences* 11 4271–88
- Frankenberg C *et al* 2011 New global observations of the terrestrial carbon cycle from GOSAT: patterns of plant fluorescence with gross primary productivity *Geophys. Res. Lett.* **38** L17706
- Funk D W, Noel L E and Freedman A H 2004 Environmental gradients, plant distribution and species richness in arctic salt marsh near Prudhoe Bay, Alaska Wetl. Ecol. Manag. 12 215–33
- Goetz S, Kimball J, Mack M and Kasischke E 2011 Scoping completed for an experiment to assess vulnerability of Arctic and boreal ecosystems *Eos Trans. Am. Geophys. Union* 92 150–1
- Gorelick N, Hancher M, Dixon M, Ilyushchenko S, Thau D and Moore R 2017 Google Earth Engine: planetary-scale

- geospatial analysis for everyone *Remote Sens. Environ.* **202** 18–27
- Griffith P C, Goetz S J, Kasischke E S, Mack M C and Wickland D E 2012 The Arctic-Boreal vulnerability experiment: a NASA terrestrial ecology field campaign *AGU Fall Meeting Abstracts* vol 2012 pp B21D–0381 (available at: https://ui.adsabs.harvard.edu/abs/2012AGUFM. B21D0381G)
- Guanter L *et al* 2014 Global and time-resolved monitoring of crop photosynthesis with chlorophyll fluorescence *Proc. Natl Acad. Sci.* 111 E1327–33
- Guanter L, Frankenberg C, Dudhia A, Lewis P E, Gómez-Dans J, Kuze A, Suto H and Grainger R G 2012 Retrieval and global assessment of terrestrial chlorophyll fluorescence from GOSAT space measurements *Remote Sens. Environ*. 121 236–51
- Hagen S C, Braswell B H, Linder E, Frolking S, Richardson A D and Hollinger D Y 2006 Statistical uncertainty of eddy flux-based estimates of gross ecosystem carbon exchange at Howland Forest, Maine *J. Geophys. Res.* 111
- Hall D K and Riggs G A 2021 MODIS/Terra snow cover 8-day L3 global 0.05Deg CMG, version 61 (https://doi.org/10.5067/MODIS/MOD10C2.061)
- Hobbie J E, Shaver G R, Rastetter E B, Cherry J E, Goetz S J, Guay K C, Gould W A and Kling G W 2017 Ecosystem responses to climate change at a Low Arctic and a High Arctic long-term research site *Ambio* 46 160–73
- Huemmrich K Fred, Vargas Zesati S, Campbell P and Tweedie C 2021 Canopy reflectance models illustrate varying NDVI responses to change in high latitude ecosystems *Ecol. Appl.* 31 e02435
- Jiang Z, Chen Y, Li J and Dou W 2005 The impact of spatial resolution on NDVI over heterogeneous surface *Proc.*. 2005 *IEEE Int. Geoscience and Remote Sensing Symp.* (2005 *IGARSS* '05) vol 2 pp 1310–3 (https://doi.org/10.1109/IGARSS.2005.1525361)
- Jiang Z, Huete A R, Chen J, Chen Y, Li J, Yan G and Zhang X 2006 Analysis of NDVI and scaled difference vegetation index retrievals of vegetation fraction *Remote Sens. Environ*. 101 366–78
- Jin H, Jönsson A M, Bolmgren K, Langvall O and Eklundh L 2017 Disentangling remotely-sensed plant phenology and snow seasonality at northern Europe using MODIS and the plant phenology index *Remote Sens. Environ.* 198 203–12
- Joiner J, Yoshida Y, Zhang Y, Duveiller G, Jung M, Lyapustin A, Wang Y and Tucker C 2018 Estimation of terrestrial global gross primary production (GPP) with satellite data-driven models and eddy covariance flux data Remote Sens. 10 1346
- Jung M et al 2020 Scaling carbon fluxes from eddy covariance sites to globe: synthesis and evaluation of the FLUXCOM approach Biogeosciences 17 1343–65
- Keenan T F, Carbone M S, Reichstein M and Richardson A D 2011 The model-data fusion pitfall: assuming certainty in an uncertain world *Oecologia* **167** 587–97
- Kobayashi H, Ikawa H and Suzuki R 2016 AmeriFlux AmeriFlux US-Prr poker flat research range Black spruce forest (https://doi.org/10.17190/AMF/1246153)
- Kobayashi H and Iwabuchi H 2008 A coupled 1-D atmosphere and 3-D canopy radiative transfer model for canopy reflectance, light environment and photosynthesis simulation in a heterogeneous landscape *Remote Sens*. *Environ.* **112** 173–85
- Kobayashi H, Suzuki R and Kobayashi S 2007 Reflectance seasonality and its relation to the canopy leaf area index in an eastern Siberian larch forest: multi-satellite data and radiative transfer analyses *Remote Sens. Environ.* **106** 238–52
- Köhler P, Frankenberg C, Magney T S, Guanter L, Joiner J and Landgraf J 2018 Global retrievals of solar-induced chlorophyll fluorescence with TROPOMI: first results and intersensor comparison to OCO-2 *Geophys. Res. Lett.* 45 10456–63
- Kreyling J 2020 The ecological importance of winter in temperate, Boreal, and Arctic ecosystems in times of climate change

- Progress in Botany vol 81, ed F M Cánovas, U Lüttge, C Leuschner and M C Risueño (Cham: Springer International Publishing) pp 377–99
- Li X *et al* 2018 Solar-induced chlorophyll fluorescence is strongly correlated with terrestrial photosynthesis for a wide variety of biomes: first global analysis based on OCO-2 and flux tower observations *Glob. Change Biol.* 24 3990–4008
- Li X and Xiao J 2022 TROPOMI observations allow for robust exploration of the relationship between solar-induced chlorophyll fluorescence and terrestrial gross primary production *Remote Sens. Environ.* **268** 112748
- Liu Y, Chen J M, He L, Zhang Z, Wang R, Rogers C, Fan W, de Oliveira G and Xie X 2022 Non-linearity between gross primary productivity and far-red solar-induced chlorophyll fluorescence emitted from canopies of major biomes *Remote Sens. Environ.* 271 112896
- Loboda T, Hoy E and Carroll M 2017 ABoVE: study domain and standard reference grids, version 2 2.049851 MB (ORNL Distributed Active Archive Center) (https://doi.org/10.3334/ ORNLDAAC/1527)
- Loisel J et al 2021 Expert assessment of future vulnerability of the global peatland carbon sink Nat. Clim. Change 11 70–77
- Magney T et al 2019 Mechanistic evidence for tracking the seasonality of photosynthesis with solar-induced fluorescence Proc. Natl Acad. Sci. 116 11640–5
- Maguire A J, Eitel J U H, Magney T S, Frankenberg C, Köhler P, Orcutt E L, Parazoo N C, Pavlick R and Pierrat Z A 2021 Spatial covariation between solar-induced fluorescence and vegetation indices from Arctic-Boreal landscapes *Environ*. Res. Lett. 16 095002
- McGuire A D, Anderson L G, Christensen T R, Dallimore S, Guo L, Hayes D J, Heimann M, Lorenson T D, Macdonald R W and Roulet N 2009 Sensitivity of the carbon cycle in the Arctic to climate change *Ecol. Monogr.* 79 523–55
- Mishra U and Riley W J 2012 Alaskan soil carbon stocks: spatial variability and dependence on environmental factors Biogeosciences 9 3637–45
- Muster S, Heim B, Abnizova A and Boike J 2013 Water body distributions across scales: a remote sensing based comparison of three Arctic tundra wetlands *Remote Sens*. 5 1498–523
- Myers-Smith I H *et al* 2020 Complexity revealed in the greening of the Arctic *Nat. Clim. Change* **10** 106–17
- NEON 2022 Bundled data products—eddy covariance (DP4.00200.001): RELEASE-2022 (https://doi.org/10.48443/7COP-3J73)
- Oechel W C, Laskowski C A, Burba G, Gioli B and Kalhori A A M 2014 Annual patterns and budget of CO₂ flux in an Arctic tussock tundra ecosystem *J. Geophys. Res.: Biogeosci.* 119 323–39
- Pallandt M T A, Kumar J, Mauritz M, Schuur E A G, Virkkala A-M, Celis G, Hoffman F M and Göckede M 2022 Representativeness assessment of the pan-Arctic eddy covariance site network and optimized future enhancements *Biogeosciences* 19 559–83
- Papale D *et al* 2015 Effect of spatial sampling from European flux towers for estimating carbon and water fluxes with artificial neural networks *J. Geophys. Res.: Biogeosci.* **120** 1941–57
- Paw U K T, Baldocchi D D, Meyers T P and Wilson K B 2000 Correction Of eddy-covariance measurements incorporating both advective effects and density fluxes Bound.-Layer Meteorol. 97 487–511
- Pierrat Z et al 2022 Diurnal and seasonal dynamics of solar-induced chlorophyll fluorescence, vegetation indices and gross primary productivity in the Boreal forest J. Geophys. Res.: Biogeosci. 127 e2021JG006588
- Pierrat Z and Stutz J 2022 Tower-based solar-induced fluorescence and vegetation index data for Southern Old Black Spruce forest (https://doi.org/10.5281/ZENODO.5884643)
- Post E *et al* 2019 The polar regions in a 2 °C warmer world *Sci. Adv.* **5** eaaw9883

- Prock S and Körner C 1996 A cross-continental comparison of phenology, leaf dynamics and dry matter allocation in Arctic and temperate zone herbaceous plants from contrasting altitudes *Ecol. Bull.* **45** 93–103 (available at: www.jstor.org/stable/20113187)
- Riihimäki H, Heiskanen J and Luoto M 2017 The effect of topography on Arctic-Alpine above ground biomass and NDVI patterns *Int. J. Appl. Earth Obs. Geoinf.* **56** 44–53
- Rocha A, Shaver G and Hobbie J 2016a AmeriFlux AmeriFlux US-An3 Anaktuvuk river unburned (https://doi.org/10. 17190/AMF/1246144)
- Rocha A V, Shaver G and Hobbie J 2016b AmeriFlux AmeriFlux US-An1 Anaktuvuk river severe burn (https://doi.org/10. 17190/AMF/1246142)
- Roland C A, Schmidt J H, Winder S G, Stehn S E and Nicklen E F 2019 Regional variation in interior Alaskan Boreal forests is driven by fire disturbance, topography and climate *Ecol. Monogr.* 89 e01369
- Roland C, Schmidt J H, Stehn S E, Hampton-Miller C J and Nicklen E F 2021 Borealization and its discontents: drivers of regional variation in plant diversity across scales in interior Alaska *Ecosphere* 12 e03485
- Running S W, Nemani R R, Heinsch F A, Zhao M, Reeves M and Hashimoto H 2004 A continuous satellite-derived measure of global terrestrial primary production *Bio Sci.* 54 547
- Ryu Y, Berry J A and Baldocchi D D 2019 What is global photosynthesis? History, uncertainties and opportunities *Remote Sens. Environ.* **223** 95–114
- Sonnentag O 2021 AmeriFlux AmeriFlux CA-SMC Smith Creek (https://doi.org/10.17190/AMF/1767830)
- Sonnentag O and Marsh P 2021a AmeriFlux AmeriFlux CA-HPC Havikpak Creek (https://doi.org/10.17190/AMF/1773392)
- Sonnentag O and Marsh P 2021b AmeriFlux AmeriFlux CA-TVC Trail valley Creek (https://doi.org/10.17190/AMF/1767831)
- Stow D A *et al* 2004 Remote sensing of vegetation and land-cover change in Arctic Tundra Ecosystems *Remote Sens. Environ.* **89** 281–308
- Sun Y *et al* 2017 OCO-2 advances photosynthesis observation from space via solar-induced chlorophyll fluorescence *Science* 358 eaam5747
- Tramontana G et al 2016 Predicting carbon dioxide and energy fluxes across global FLUXNET sites with regression algorithms *Biogeosciences* 13 4291–313
- Tramontana G, Ichii K, Camps-Valls G, Tomelleri E and Papale D 2015 Uncertainty analysis of gross primary production upscaling using random forests, remote sensing and eddy covariance data *Remote Sens. Environ.* **168** 360–73
- Turner A J, Köhler P, Magney T S, Frankenberg C, Fung I and Cohen R C 2020 A double peak in the seasonality of California's photosynthesis as observed from space *Biogeosciences* 17 405–22
- Turner A J, Köhler P, Magney T S, Frankenberg C, Fung I and Cohen R C 2021 Extreme events driving year-to-year differences in gross primary productivity across the US Biogeosciences 18 6579–88
- Virkkala A-M *et al* 2022 The ABCflux database: Arctic–boreal CO₂ flux observations and ancillary information aggregated to monthly time steps across terrestrial ecosystems *Earth Syst. Sci. Data* 14 179–208
- Walsh J E and Brettschneider B 2019 Attribution of recent warming in Alaska *Polar Sci.* 21 101–9
- Walther S, Guanter L, Heim B, Jung M, Duveiller G, Wolanin A and Sachs T 2018 Assessing the dynamics of vegetation productivity in circumpolar regions with different satellite indicators of greenness and photosynthesis *Biogeosciences* 15 6221–56
- Walther S, Voigt M, Thum T, Gonsamo A, Zhang Y, Köhler P, Jung M, Varlagin A and Guanter L 2016 Satellite chlorophyll fluorescence measurements reveal large-scale decoupling of photosynthesis and greenness dynamics in Boreal evergreen forests *Glob. Change Biol.* 22 2979–96

- Wang J A, Sulla-Menashe D, Woodcock C E, Sonnentag O, Keeling R F and Friedl M A 2020 Extensive land cover change across Arctic–Boreal Northwestern North America from disturbance and climate forcing Glob. Change Biol. 26 807–22
- Wang J A, Sulla-Menashe D, Woodcock C, Sonnentag O, Keeling R and Friedl M 2019 ABoVE: landsat-derived annual dominant land cover across ABoVE core domain, 1984–2014 (https://doi.org/10.3334/ORNLDAAC/1691)
- Wu D, Lin J C, Duarte H F, Yadav V, Parazoo N C, Oda T and Kort E A 2021 A model for urban biogenic CO₂ fluxes: solar-induced fluorescence for modeling urban biogenic fluxes (SMUrF v1) Geosci. Model Dev. 14 3633–61
- Wu G et al 2022 Attributing differences of solar-induced chlorophyll fluorescence (SIF)-gross primary production (GPP) relationships between two C4 crops: corn and miscanthus Agric. For. Meteorol. 323 109046
- Wutzler T, Lucas-Moffat A, Migliavacca M, Knauer J, Sickel K, Šigut L, Menzer O and Reichstein M 2018 Basic and extensible post-processing of eddy covariance flux data with REddyProc *Biogeosciences* 15 5015–30

- Xiao J, Davis K J, Urban N M and Keller K 2014 Uncertainty in model parameters and regional carbon fluxes: a model-data fusion approach Agric. For. Meteorol. 189–190 175–86
- Zeng Y, Badgley G, Dechant B, Ryu Y, Chen M and Berry J A 2019 A practical approach for estimating the escape ratio of near-infrared solar-induced chlorophyll fluorescence *Remote Sens. Environ.* 232 111209
- Zhang Z et al 2020 Reduction of structural impacts and distinction of photosynthetic pathways in a global estimation of GPP from space-borne solar-induced chlorophyll fluorescence Remote Sens. Environ. 240 111722
- Zhao M, Heinsch F A, Nemani R R and Running S W 2005 Improvements of the MODIS terrestrial gross and net primary production global data set *Remote Sens. Environ*. 95 164–76
- Zona D *et al* 2022 Earlier snowmelt may lead to late season declines in plant productivity and carbon sequestration in Arctic tundra ecosystems *Sci. Rep.* 12 3986
- Zona D and Oechel W 2016 AmeriFlux AmeriFlux US-Ivo Ivotuk (https://doi.org/10.17190/AMF/1246067)